

Nodal High-Order Discontinuous Galerkin Methods for the Spherical Shallow Water Equations

F. X. Giraldo^{†1}, J. S. Hesthaven[‡] and T. Warburton^{*}

[†]*Naval Research Laboratory, Monterey, CA 93943*

[‡]*Division of Applied Mathematics, Brown University, Providence, RI 02912*

^{*}*Dept. of Mathematics and Statistics, University of New Mexico, Albuquerque, NM 87131*

We develop and evaluate a high-order discontinuous Galerkin method for the solution of the shallow water equations on the sphere. To overcome well known problems with polar singularities, we consider the shallow water equations in Cartesian coordinates, augmented with a Lagrange multiplier to ensure that fluid particles are constrained to the spherical surface.

The global solutions are represented by a collection of curvilinear quadrilaterals from an icosahedral grid. On each of these elements the local solutions are assumed to be well approximated by a high-order nodal Lagrange polynomial, constructed from a tensor-product of the Legendre-Gauss-Lobatto points which also supplies a high-order quadrature. The shallow water equations are satisfied in a local discontinuous element fashion with solution continuity being enforced weakly.

The numerical experiments, involving a comparison of weak and strong conservation forms as well as the impact of over-integration, confirm the expected high-order accuracy and the potential for using such highly parallel formulations in numerical weather prediction.

Key Words: discontinuous Galerkin method, high-order, icosahedral grid, shallow water equations, spectral element method, spherical geometry.

1. INTRODUCTION

The majority of current climate and numerical weather prediction (NWP) models, e.g., the operational NWP models developed by the European Center for Medium-Range Weather Forecasting (ECMWF), the National Center for Environmental Prediction (NCEP), and the Naval Research Laboratory (NRL), are based on globally defined spectral methods [11, 14, 24, 25]. While these methods continue to be essential tools for NWP, their limitations are beginning to emerge. For one, the fixed global grid makes adaptive solution techniques very complex if possible at

¹Corresponding Author

Report Documentation Page				Form Approved OMB No. 0704-0188	
Public reporting burden for the collection of information is estimated to average 1 hour per response, including the time for reviewing instructions, searching existing data sources, gathering and maintaining the data needed, and completing and reviewing the collection of information. Send comments regarding this burden estimate or any other aspect of this collection of information, including suggestions for reducing this burden, to Washington Headquarters Services, Directorate for Information Operations and Reports, 1215 Jefferson Davis Highway, Suite 1204, Arlington VA 22202-4302. Respondents should be aware that notwithstanding any other provision of law, no person shall be subject to a penalty for failing to comply with a collection of information if it does not display a currently valid OMB control number.					
1. REPORT DATE 2001		2. REPORT TYPE		3. DATES COVERED 00-00-2001 to 00-00-2001	
4. TITLE AND SUBTITLE Nodal High-Order Discontinuos Galerkin Methods for the Spherical Shallow Water Equations				5a. CONTRACT NUMBER	
				5b. GRANT NUMBER	
				5c. PROGRAM ELEMENT NUMBER	
6. AUTHOR(S)				5d. PROJECT NUMBER	
				5e. TASK NUMBER	
				5f. WORK UNIT NUMBER	
7. PERFORMING ORGANIZATION NAME(S) AND ADDRESS(ES) Brown University,Division of Applied Mathematics,182 George Street,Providence,RI,02912				8. PERFORMING ORGANIZATION REPORT NUMBER	
9. SPONSORING/MONITORING AGENCY NAME(S) AND ADDRESS(ES)				10. SPONSOR/MONITOR'S ACRONYM(S)	
				11. SPONSOR/MONITOR'S REPORT NUMBER(S)	
12. DISTRIBUTION/AVAILABILITY STATEMENT Approved for public release; distribution unlimited					
13. SUPPLEMENTARY NOTES The original document contains color images.					
14. ABSTRACT					
15. SUBJECT TERMS					
16. SECURITY CLASSIFICATION OF:			17. LIMITATION OF ABSTRACT	18. NUMBER OF PAGES 25	19a. NAME OF RESPONSIBLE PERSON
a. REPORT unclassified	b. ABSTRACT unclassified	c. THIS PAGE unclassified			

all. Furthermore, the recent paradigm shift in large-scale computing from vector to distributed-memory computing platforms has exposed problems with achieving efficiency due to the global, inter-processor, all-to-all communication needed in the spectral transform.

Such considerations have stimulated research into parallel methods and potentially adaptive methods, suitable for NWP, yet maintaining the accuracy of the global spectral approach while overcoming its inherent limitations.

Continuous spectral element methods have recently been proposed for future climate [26] and NWP [9] models. In these methods the solution is first constructed in a local element-by-element manner and then a portion of this local solution is distributed to the global grid points shared by adjacent elements. This global assembly from the elements to the global grid points is what enforces continuity and it is this requirement which reduces the locality of the method. Although continuous spectral element methods parallelize quite well [27] their insistence on continuity makes them cumbersome to employ in either a non-conforming approach [17] or in an adaptive solution strategy.

In this paper we introduce a nodal high-order discontinuous Galerkin method for geophysical flows on the sphere. Like continuous spectral element methods, discontinuous Galerkin methods (DGM) can be constructed to have high-order accuracy, while maintaining a large degree of locality, hence enabling high parallel performance and adaptive solution procedures. The locality of these methods ensures that they can be used with any type of grid, e.g., unstructured and non-conforming if needed. In this paper we shall demonstrate this by using unstructured icosahedral grids.

As a first step towards the construction of a fully 3D atmospheric model we demonstrate the efficiency and accuracy of the nodal high-order DGM by solving the shallow water equations on the sphere. The shallow water equations contain all of the horizontal operators required in an atmospheric model and thus represent a good first test for newly proposed methods for atmospheric models.

The remainder of the paper is organized as follows. In Sec. 2 we introduce the spherical shallow water equations and discuss the reasons for using a Cartesian grid. This sets the stage for Sec. 3 which introduces the numerical scheme and discusses in detail the spatial curvilinear representation of the solution as well as the formulation enabling one to satisfy the equations in a discontinuous fashion. We also discuss the temporal time-stepping scheme and the approach taken to generate a suitable grid on the sphere. In Sec. 4 we demonstrate the accuracy, efficiency, and robustness of the complete scheme for the solution of benchmark problems for the spherical shallow water equations. Section 5 contains a few remarks and outlines natural extensions of the work presented here.

2. SPHERICAL SHALLOW WATER EQUATIONS

The spherical shallow water equations in conservation form are given as

$$\frac{\partial \mathbf{q}}{\partial t} + \nabla \cdot \mathbf{F}(\mathbf{q}) = \mathbf{S}(\mathbf{x}, \mathbf{q}) , \quad (1)$$

where

$$\mathbf{q} = [\varphi, \varphi u, \varphi v, \varphi w]^T ,$$

represents the state vector, \mathbf{q} , composed of the geopotential height, φ , and the three Cartesian velocity components, (u, v, w) , all being a function of $\mathbf{x} \in \mathbb{R}^3$ and time, t . The units for φ and \mathbf{u} are $(\text{m/s})^2$ and m/s , respectively.

The flux, $\mathbf{F}(\mathbf{q})$, takes the form

$$\mathbf{F}(\mathbf{q}) = \begin{bmatrix} \varphi u \\ \varphi u^2 + \frac{1}{2}\varphi^2 \\ \varphi uv \\ \varphi uw \end{bmatrix} \hat{\mathbf{i}} + \begin{bmatrix} \varphi v \\ \varphi uv \\ \varphi v^2 + \frac{1}{2}\varphi^2 \\ \varphi vw \end{bmatrix} \hat{\mathbf{j}} + \begin{bmatrix} \varphi w \\ \varphi uw \\ \varphi vw \\ \varphi w^2 + \frac{1}{2}\varphi^2 \end{bmatrix} \hat{\mathbf{k}} , \quad (2)$$

where $(\hat{\mathbf{i}}, \hat{\mathbf{j}}, \hat{\mathbf{k}})$ represent the Cartesian unit vectors. The source term, $\mathbf{S}(\mathbf{x}, \mathbf{q})$, in Eq.(1), acting only on the momentum equations, is given as

$$\mathbf{S}(\mathbf{x}, \mathbf{q}) = -\frac{2\Omega\varphi}{R^2}\mathbf{x} \times \mathbf{u} - \varphi\nabla\varphi_s + \mu\mathbf{x} .$$

Here the first term accounts for the Coriolis force, with $R = 6.371 \times 10^6$ m being the radius and $\Omega = 7.292 \times 10^{-5}$ rad/s the angular frequency of the earth, while the second contribution models the effects of a variable surface height through the surface potential, φ_s . The last term is a Lagrange multiplier, the specification of which we shall return to shortly.

Equation (1) is derived from the incompressible and inviscid Navier-Stokes equations by vertically integrating the mass to yield the geopotential height equation (for further details see [22]). Contrary to most other work on the numerical solution of Eq.(1) on a spherical shell, we shall not recast it in spherical coordinates but rather maintain the Cartesian coordinates. The main motivation for doing so, albeit at the expense of introducing an additional momentum equation, is to avoid the problems associated with the polar singularity. For a spherical shell, described by the coordinates (λ, θ) , of radius R the divergence of a vector field, $\mathbf{F} = f\hat{\lambda} + g\hat{\theta}$, is given as

$$\nabla \cdot \mathbf{F} = \frac{1}{R \cos \theta} \left[\frac{\partial f}{\partial \lambda} + \frac{\partial g \cos \theta}{\partial \theta} \right] .$$

At the poles, i.e., $\theta = \pm\pi/2$, this is a source of numerical problems, caused by the specific formulation rather than the nature of the shallow water equations and its solutions. While the use of a local Cartesian coordinate system has been used to overcome these problems in the past [26] we have, guided by the results of previous work [9], chosen to maintain the Cartesian formulation everywhere.

To ensure that the fluid particles remain on the spherical shell, we require that the fluid velocity remains perpendicular to the position vector, i.e., $\mathbf{x} \cdot \mathbf{u} = 0$, which yields the Lagrange multiplier

$$\mu(\mathbf{x}, \mathbf{q}) = \frac{1}{R^2} \left[\varphi \mathbf{x} \cdot \nabla \varphi_s + \mathbf{x} \cdot (\nabla \cdot \tilde{\mathbf{F}}) \right] . \quad (3)$$

Here $\tilde{\mathbf{F}}$ represents the parts of the flux, Eq. (2), associated with the momentum equations, i.e., the last three fluxes. Note that the term associated with the Coriolis term vanishes identically at this exact level while this may not be case at the discrete level. As no constraint is needed on the geophysical potential, essentially representing the local mass, the multiplier is needed in the momentum equations only.

3. THE NUMERICAL SCHEME

In developing the numerical scheme for the solution of Eq. (1) we shall split the discussion into a treatment of the spatial discretization and the approximation of the resulting semi-discrete approximation.

3.1. The Spatial Approximation

The discussion of the spatial approximation scheme involves, as does any formulation of a scheme for solving partial differential equations, attention to the questions of how to represent the solution as well as in which way the equations are required to be satisfied. In the following we address these two issues in more detail.

3.1.1. Representing the Solution and Basic Operations

Initially, we assume that the computational domain, S , i.e., a spherical shell, is covered by K non-overlapping curvilinear quadrilaterals, D , such that

$$S = \bigcup_{k=1}^K D^k .$$

The construction of this sphere covering is not entirely trivial and we shall return to this problem in Sec. 4. For now, however, we simply assume its existence.

To enable the efficient and accurate computation of operations such as differentiation and integration, we introduce a nonsingular mapping, $\mathbf{x} = \Psi(\boldsymbol{\xi})$, which connects the local physical coordinates, $\mathbf{x} = (x, y, z)$, defined on D with a reference system $\boldsymbol{\xi} = (\xi, \eta, \zeta)$, defined on the local element such that (ξ, η) lies on the spherical surface. Thus, ζ represents the spherical radius vector itself, i.e., ζ constant corresponds to a shell of a constant radius. For simplicity we assume that $(\xi, \eta) \in [-1, 1]^2$ on each element, see Fig. 1.

Associated with the local mapping, Ψ , is the transformation Jacobian, $J = \frac{\partial \mathbf{x}}{\partial \boldsymbol{\xi}}$, and the determinant

$$|J| = \frac{\partial \mathbf{x}}{\partial \zeta} \cdot \mathbf{G} , \quad \mathbf{G} = \frac{\partial \mathbf{x}}{\partial \xi} \times \frac{\partial \mathbf{x}}{\partial \eta} ,$$

where \mathbf{G} represents the surface conforming component of the mapping (see [9] for further details).

The mapping also supplies the local metric, $\nabla \xi$ and $\nabla \eta$, as well as the local normal vectors at the surface of the element. Indeed, as illustrated in Fig. 1, the normals are given as

$$\hat{\mathbf{n}} = \eta \frac{\nabla \eta}{|\nabla \eta|} \Big|_{\eta=\pm 1} , \quad \hat{\mathbf{n}} = \xi \frac{\nabla \xi}{|\nabla \xi|} \Big|_{\xi=\pm 1} ,$$

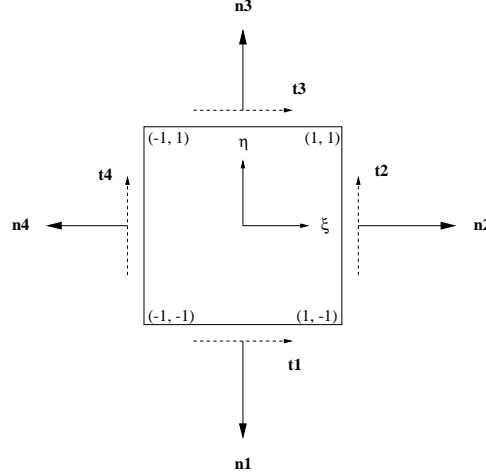


FIG. 1. The geometry of the mapping and the associated metric information.

for the sides 1/3 and 2/4, respectively.

With this in place we can now focus on the local element-wise representation of the solution, \mathbf{q} , and the approximation of operations such as differentiation and integration. For simplicity, we assume ζ to be unity in what remains and denote $\boldsymbol{\xi} = (\xi, \eta)$ unless clarification is deemed necessary.

The simple structure of the standard element, \mathbf{l} , spanned by $\boldsymbol{\xi} \in [-1, 1]^2$, makes it natural to represent the local solution by an N th order polynomial in $\boldsymbol{\xi}$ as

$$\mathbf{q}_N(\mathbf{x}) = \sum_{k=1}^{(N+1)^2} \mathbf{q}_N(\mathbf{x}_k) L_k(\mathbf{x}) ,$$

where \mathbf{x}_k represents $(N+1)^2$ grid points and $L_k(\mathbf{x})$ reflects the associated multivariate Lagrange interpolation polynomial. The logical square structure of \mathbf{l} simplifies matters further in that we can express the Lagrange polynomial by a tensor-product as

$$L_k(\mathbf{x}) = h_i(\xi(\mathbf{x})) h_j(\eta(\mathbf{x})) , \quad (4)$$

where $i, j = 0, \dots, N$.

While many choices of the grid points, (ξ_i, η_j) , are possible, it is natural to choose the Legendre-Gauss-Lobatto points, given as the tensor-product of the roots of

$$(1 - \xi^2) P'_N(\xi) = 0 ,$$

where $P_N(\xi)$ is the N th order Legendre polynomial. This choice is natural as these points are endowed with a Gaussian quadrature rule which shall become useful shortly. With this choice, the one-dimensional Lagrange polynomials, $h_i(\xi)$, also known as the Legendre cardinal functions, become

$$h_i(\xi) = -\frac{1}{N(N+1)} \frac{(1 - \xi^2) P'_N(\xi)}{(\xi - \xi_i) P'_N(\xi_i)} ,$$

and likewise for $h_j(\eta)$.

The choice of the Legendre-Gauss-Lobatto points enables the straightforward approximation of element-wise integrals, i.e.,

$$\int_D q(\mathbf{x}) d\mathbf{x} = \int_I q(\xi) J(\xi) d\xi \simeq \sum_{i,j=0}^N q(\xi_i, \eta_j) J(\xi_i, \eta_j) \omega_i^\xi \omega_j^\eta ,$$

where J represents the local Jacobian for the transformation between D and I , and ω_i^ξ and ω_j^η are the Gaussian quadrature weights,

$$\omega_i^\xi = \frac{2}{N(N+1)} \left(\frac{1}{P_N(\xi_i)} \right)^2 ,$$

associated with the one dimensional Legendre-Gauss-Lobatto quadrature. We recall that if qJ is a polynomial of at most degree $2N-1$ in each local coordinate, the quadrature is exact.

The evaluation of surface integrals, made particularly simple by the natural separation between interior and edge (side) nodes in the nodal formulation considered here, follows the same line of thinking, i.e.,

$$\begin{aligned} \oint_{\delta D} q(\mathbf{x}) d\mathbf{x} &= \oint_{\delta I} q(\xi) J(\xi) d\xi \\ &\simeq \sum_{i=0}^N [q(\xi_i, -1) J(\xi_i, -1) + q(\xi_i, 1) J(\xi_i, 1)] \omega_i^\xi \\ &\quad + \sum_{j=0}^N [q(-1, \eta_j) J(-1, \eta_j) + q(1, \eta_j) J(1, \eta_j)] \omega_j^\eta . \end{aligned}$$

3.1.2. Satisfying the Equation

With the local representation of the solutions and the central operations in place, we shall now proceed to consider the question of how to satisfy the equation. We assume that the solution, \mathbf{q} , to Eq.(1) is represented locally by high-order polynomials, \mathbf{q}_N , defined on the curvilinear quadrilateral, D , and require that the equation be satisfied element-wise in the following discontinuous Galerkin way

$$\int_D \left(\frac{\partial \mathbf{q}_N}{\partial t} + \nabla \cdot \mathbf{F}_N - \mathbf{S}_N \right) L_k(\mathbf{x}) d\mathbf{x} = \oint_{\delta D} L_k(\mathbf{x}) \hat{\mathbf{n}} \cdot [\mathbf{F}_N - \mathbf{F}_N^*] d\mathbf{x} , \quad (5)$$

where $L_k(\mathbf{x})$ ($k \in [1, \dots, (N+1)^2]$) is the local polynomial basis, Eq.(4). We have also introduced the polynomial representation of the flux, $\mathbf{F}_N = \mathbf{F}_N(\mathbf{q}_N)$, and the source, $\mathbf{S}_N = \mathbf{S}_N(\mathbf{x}, \mathbf{q}_N)$, as

$$\mathbf{F}_N(\mathbf{q}_N) = \sum_{k=1}^{(N+1)^2} \mathbf{F}(\mathbf{q}_N(\mathbf{x}_k)) L_k(\mathbf{x}) , \quad \mathbf{S}_N(\mathbf{x}, \mathbf{q}_N) = \sum_{k=1}^{(N+1)^2} \mathbf{S}(\mathbf{x}_k, \mathbf{q}_N(\mathbf{x}_k)) L_k(\mathbf{x}) .$$

The numerical flux, \mathbf{F}_N^* , in Eq.(5) shall be discussed in detail shortly. Prior to that, however, a few remarks concerning Eq.(5), are in order. First of all we note that the interface conditions, introduced into the formulation through the numerical flux, are enforced only weakly, i.e., the solution is in general discontinuous. As we shall see, however, this does not impact the accuracy as the size of the jump vanishes to the order of the interior approximation. Furthermore, the discontinuous formulation ensures a highly parallel scheme as all communication is local between elements sharing edges in two-dimensions or faces in three-dimensions. Finally, the locality of the approximation makes it straightforward to extend the scheme to include support for different orders of approximations in different elements, non-conforming or different types of elements, e.g., triangles and quadrilaterals.

Before discussing the numerical flux, let us note that a mathematically equivalent but numerically different formulation of Eq.(5) can be obtained by an integration by parts to recover

$$\int_D \left(\frac{\partial \mathbf{q}_N}{\partial t} - \mathbf{F}_N \cdot \nabla - \mathbf{S}_N \right) L_k(\mathbf{x}) d\mathbf{x} = - \oint_{\partial D} L_k(\mathbf{x}) \mathbf{F}_N^* d\mathbf{x} . \quad (6)$$

This can be recognized as the classical discontinuous Galerkin method for conservation laws [1, 2, 4, 18]. To distinguish between the two formulations, we shall refer to Eq.(5) as the divergence form and the more familiar one, Eq.(6), as Green's form. Other terms often used to describe these formulations are the strong and the weak form, respectively.

The numerical flux, \mathbf{F}_N^* , is the part of the formulation that allows information to be passed between the individual elements, the union of which forms S . The discontinuous formulation implies that the solution at an interface is non-unique and we must ensure that a unique solution be identified and passed to both elements in a way consistent with the dynamics of the problem.

This is a situation similar to a classical finite volume formulation to which Eq.(6) reduces for the lowest order elements. Thus, we can borrow from the extensive literature devoted to the development and analysis of numerical fluxes within the context of finite volume methods, e.g., upwinding by linearization or approximate Riemann solvers such as Roe [23], Engquist-Osher [6] or Van Leer [28] fluxes.

For simplicity and generality we use subsequently the simple Lax-Friedrichs flux of the form

$$\mathbf{F}_N^* = \frac{\mathbf{F}_N(\mathbf{q}_N) + \mathbf{F}_N(\mathbf{p}_N)}{2} - \frac{|\lambda|}{2} (\mathbf{p}_N - \mathbf{q}_N) ,$$

where \mathbf{q}_N refers to the local computed solution and \mathbf{p}_N refers to the solution in the neighboring element. The dissipative term is scaled by $|\lambda|$ which represents the maximum (local) eigenvalue of the flux Jacobian

$$\frac{\partial \hat{\mathbf{n}} \cdot \mathbf{F}}{\partial \mathbf{q}} = \begin{bmatrix} 0 & \hat{n}_x & \hat{n}_y & \hat{n}_z \\ \hat{n}_x \varphi - uU & \hat{n}_x u + U & \hat{n}_y u & \hat{n}_z u \\ \hat{n}_y \varphi - vU & \hat{n}_x v & \hat{n}_y v + U & \hat{n}_z v \\ \hat{n}_z \varphi - wU & \hat{n}_x w & \hat{n}_y w & \hat{n}_z w + U \end{bmatrix} ,$$

where

$$U = \hat{\mathbf{n}} \cdot \mathbf{u} \ .$$

The eigenvalues of the flux Jacobian are $\Lambda = [U, U, U + \sqrt{\varphi}, U - \sqrt{\varphi}]^T$, such that

$$|\lambda| = |U| + \sqrt{\varphi} \ ,$$

is the maximum wave speed of the shallow water equations entering the Lax-Friedrichs flux. While it is well known that the use of a Lax-Friedrichs flux in a classical finite volume formulation leads to a very dissipative scheme, this is much less of a problem in a high-order formulation where the quality of the numerical flux is less critical [5].

To simplify matters further for both formulations, let us introduce

$$\mathbf{M}_{lk} = \int_{\mathbf{D}} L_l(\mathbf{x}) L_k(\mathbf{x}) d\mathbf{x} \ , \ \mathbf{D}_{lk} = \int_{\mathbf{D}} L_l(\mathbf{x}) \nabla L_k(\mathbf{x}) d\mathbf{x} \ , \quad (7)$$

as the mass matrix and the differentiation operator, respectively. Note that $\mathbf{D} = [\mathbf{D}^x, \mathbf{D}^y, \mathbf{D}^z]$ is a vector of matrices corresponding to a discrete gradient operator. To account for the source we define

$$\mathbf{S}_{lk} = \frac{2\Omega}{R^2} \sum_{m=1}^{(N+1)^2} \mathbf{x}_m \int_{\mathbf{D}} L_m(\mathbf{x}) L_l(\mathbf{x}) L_k(\mathbf{x}) d\mathbf{x} \ , \ \mathbf{M}_{lk}^\varphi = \int_{\mathbf{D}} L_l(\mathbf{x}) L_k(\mathbf{x}) \nabla \varphi_s(\mathbf{x}) d\mathbf{x} \ .$$

As \mathbf{D} , both \mathbf{S} and \mathbf{M}^φ are 3-vectors of matrices.

Finally we introduce the operator associated with the surface integral as

$$\mathbf{F}_{lk} = \oint_{\partial \mathbf{D}} L_l(\mathbf{x}) L_k(\mathbf{x}) d\mathbf{x} \ ,$$

where l includes the trace of nodes on the face of \mathbf{D} only. Denoting the local element-wise grid vector of the geopotential as $\boldsymbol{\varphi}_N$ and, correspondingly, the grid vector for the three momentum components as $\boldsymbol{\varphi} \mathbf{u}_N$ and $\mathbf{q}_N = [\boldsymbol{\varphi}_N, \boldsymbol{\varphi} \mathbf{u}_N]^T$, we can now express the semi-discrete approximation of the divergence form, Eq.(5), as

$$\begin{aligned} (\mathbf{I}_4 \otimes \mathbf{M}) \frac{d}{dt} \mathbf{q}_N + \mathbf{D} \cdot \mathbf{F}_N(\mathbf{q}_N) = & - \begin{bmatrix} 0 & 0 \\ \mathbf{M}^\varphi & \mathbf{S}_\times \end{bmatrix} \mathbf{q}_N \\ & + \begin{bmatrix} 0 & 0 \\ 0 & \mu \mathbf{I}_3 \otimes \mathbf{M} \end{bmatrix} \begin{bmatrix} 0 \\ \mathbf{x}_N \end{bmatrix} + \mathbf{I}_4 \otimes \mathbf{F} [\mathbf{F}_N(\mathbf{q}_N) - \mathbf{F}^*] , \end{aligned} \quad (8)$$

where \mathbf{I}_r is a rank- r identity matrix and the Lagrange multipliers are contained in the diagonal matrix, $\mu = \text{diag}[\mu_1, \dots, \mu_{(N+1)^2}]$. Finally we have introduced the arrays of nodal physical coordinates, $\mathbf{x}_N = [x_N, y_N, z_N]^T$.

Similarly, we can express the Green's form, Eq.(6), using the above notation as

$$\begin{aligned} (\mathbf{I}_4 \otimes \mathbf{M}) \frac{d}{dt} \mathbf{q}_N - \mathbf{D}^T \cdot \mathbf{F}_N(\mathbf{q}_N) = & - \begin{bmatrix} 0 & 0 \\ \mathbf{M}^\varphi & \mathbf{S}_\times \end{bmatrix} \mathbf{q}_N \\ & + \begin{bmatrix} 0 & 0 \\ 0 & \mu \mathbf{I}_3 \otimes \mathbf{M} \end{bmatrix} \begin{bmatrix} 0 \\ \mathbf{x}_N \end{bmatrix} - (\mathbf{I}_4 \otimes \mathbf{F}) \mathbf{F}^* \ . \end{aligned} \quad (9)$$

In both cases we can compute the Lagrange multipliers in a way similar to the continuous case, Eq.(3), i.e., by requiring that the discrete momentum is pointwise normal to the position vector. Note that the effect of the Coriolis force needs to be included in the discrete form to ensure that fluid particles remain on the spherical shell.

It is worth noticing that both schemes given above are fully explicit in time, i.e., no global assembly is required in contrast to a classical finite element/spectral element scheme, and is thus parallel by construction. The only overhead associated with the above formulation is the additional memory required to store the multiple solutions at the overlapping regions of the elements, i.e., the edges (sides). For high-order elements this memory overhead is clearly negligible as the number of edge to volume nodes decreases rapidly as the order increases.

3.2. Temporal Integration and Stability

The explicit nature of the semi-discrete formulation

$$\frac{\partial \mathbf{q}_N}{\partial t} = \mathbf{B}(\mathbf{q}_N) ,$$

where \mathbf{B} signifies the operators given in Eqs.(8)-(9), makes it natural to use a standard explicit Runge-Kutta scheme. This yields

$$\forall k = 1, \dots, 3 : \quad \mathbf{q}_N^{k+1} = \mathbf{q}_N^k + \Delta t \alpha_k \mathbf{B}(\mathbf{q}_N^k) ,$$

with $\mathbf{q}_N^{k=1} = \mathbf{q}_N^n$ and

$$\mathbf{q}_N^{n+1} = \mathbf{q}_N^n + \frac{\Delta t}{6} \sum_{k=1}^4 \beta_k \mathbf{B}(\mathbf{q}_N^k) ,$$

where

$$\alpha_1 = \alpha_2 = \frac{1}{2}, \quad \alpha_3 = 1, \quad \text{and} \quad \beta_1 = \beta_4 = 1, \quad \beta_2 = \beta_3 = 2 .$$

The time step, Δt , is chosen in order to ensure a stable scheme and will generally scale like

$$\Delta t \leq \text{CFL} \times \min_{\mathbf{x} \in \mathbf{D}} [|\mathbf{u} \cdot \boldsymbol{\chi}| + \varphi \sqrt{\boldsymbol{\chi} \cdot \boldsymbol{\chi}}]^{-1} ,$$

where the local grid distortion is measured by

$$\boldsymbol{\chi} = \left(\frac{|\xi_x|}{\Delta \xi} + \frac{|\eta_x|}{\Delta \eta}, \frac{|\xi_y|}{\Delta \xi} + \frac{|\eta_y|}{\Delta \eta}, \frac{|\xi_z|}{\Delta \xi} + \frac{|\eta_z|}{\Delta \eta} \right) .$$

Here $(\Delta \xi, \Delta \eta)$ reflects the local average grid size and $\mathbf{u} = (u, v, w)$ the local velocity.

Even with a suitably chosen value of the time-step it is well known that high-order methods are prone to instabilities due to the nonlinear mixing and lack of dissipation, see e.g. [10]. This is particularly true for problems with marginally resolved phenomena where the nonlinear mixing of the solution with the Gibbs oscillations can drive the instability.

The standard approach to avoid this instability in a controlled manner is through the use of a weak high-order filter which modifies the high frequency modes without altering the well resolved low frequency modes. As has been shown over the last decade such filtering can be applied without sacrificing spectral accuracy [10, 26].

We shall focus on the filters developed by Boyd [3] and Vandeveen [29]. While these filters perform well, their use are known to pose difficulties in a classical spectral element scheme where the solution is required to be continuous. As we shall see shortly, however, these difficulties vanish in the current formulation.

Following the discussion in [3], consider the state variables, \mathbf{q}_N , as

$$\mathbf{q}_N = \sum_{k=1}^{(N+1)^2} \mathbf{q}_N(\boldsymbol{\xi}_k) L_k(\boldsymbol{\xi}) = \sum_{i,j=0}^N \hat{\mathbf{q}}_{ij} P_i(\xi) P_j(\eta) \quad ,$$

where $L_k(\boldsymbol{\xi})$ is the Lagrange polynomial associated with the points, $\boldsymbol{\xi}_k$, $P_i(\xi)$ and $P_j(\eta)$ the Legendre polynomials in ξ and η , respectively, and $\hat{\mathbf{q}}_{ij}$ the discrete Legendre expansion coefficients of the state vector computed by using the Legendre quadrature.

The filtering approach proposed in [3] involves the weighted sum

$$\mathbf{q}_N^F = (1 - \nu) \mathbf{q}_N + \nu \sum_{i,j=0}^N \sigma_i \sigma_j \hat{\mathbf{q}}_{ij} P_i(\xi) P_j(\eta) \quad , \quad (10)$$

where ν is the filter weighting, i.e., $\nu = 0$ represents no filtering and $\nu = 1$ full filtering. Furthermore

$$\sigma_i = \begin{cases} 1 & \text{for } i < s \\ \sigma\left(\frac{i-s}{N-s}\right) & \text{for } s \leq i \leq N \end{cases}$$

is the filter function with σ being the Boyd-Vandeveen filter [3]; σ_j is defined likewise. Note that the filtering is performed in an element sense. In other words, each element yields its very own set of filtered values. However, if using a spectral element formulation we would need to require that the state vector be continuous across elements. As the filtering gives different values for grid points shared by elements some form of weighting is typically required to recover continuity. Since we advocate a discontinuous element formulation, however, this correction is unnecessary, hence greatly simplifying the inclusion of filters into the schemes.

4. GENERATION OF ICOSAHEDRAL GRIDS ON THE SPHERE

Contrary to the more traditional solution techniques exploiting spherical harmonics [11, 14, 16, 24, 25], the use of a multi-element formulation allows for the use of any type of grid, e.g., not only unstructured grids but non-conforming grids as well.

The generation of the grid on the sphere is a challenging problem and in this section we describe the procedure for generation of general high order icosahedral grid proposed in [8, 9]. This grid is derived from the icosahedron comprised of 20 equilateral triangular elements and 12 grid points.

To construct icosahedral grids we consider the initial icosahedron and subdivide each of the initial triangles by a triangular Lagrange polynomial of order n_I . Prior to mapping these elements onto the sphere it is convenient to map the triangles onto a gnomonic space. The most unbiased mapping is obtained by mapping about the centroid of the triangles.

Let (λ_c, θ_c) be the centroid of the triangle we wish to map. The gnomonic mapping is then given by

$$\begin{aligned} x &= \frac{a \cos \theta \sin(\lambda - \lambda_c)}{\sin \theta_c \sin \theta + \cos \theta_c \cos \theta \cos(\lambda - \lambda_c)}, \\ y &= \frac{a [\cos \theta_c \sin \theta - \sin \theta_c \cos \theta \cos(\lambda - \lambda_c)]}{\sin \theta_c \sin \theta + \cos \theta_c \cos \theta \cos(\lambda - \lambda_c)}. \end{aligned} \quad (11)$$

To simplify matters a bit, we first apply a rotation whereby Eq.(11) becomes

$$x = a \tan \lambda', \quad y = a \tan \theta' \sec \lambda', \quad (12)$$

in the new coordinate system with the coordinates (λ, θ) located at $(0, 0)$. The rotation mapping is given as

$$\begin{aligned} \lambda' &= \arctan \left[\frac{\cos \theta \sin(\lambda - \lambda_c)}{\sin \theta_c \sin \theta + \cos \theta_c \cos \theta \cos(\lambda - \lambda_c)} \right], \\ \theta' &= \arcsin [\cos \theta_c \sin \theta - \sin \theta_c \cos \theta \cos(\lambda - \lambda_c)]. \end{aligned} \quad (13)$$

This approach enables the construction of a general icosahedral grid defined by

$$\begin{aligned} N_p^T &= 10(n_I - 1)^2 + 20(n_I - 1) + 12, \\ N_e^T &= 2(N_p^T - 2), \\ N_s^T &= 3(N_p^T - 2), \end{aligned} \quad (14)$$

where N_p^T, N_e^T , and N_s^T denote the number of points, elements, and sides comprising the triangular grid.

Once the triangular icosahedral grid is constructed, we subdivide each triangular element into 3 quadrilateral elements. Upon dividing the triangles into quadrilaterals one can construct the higher order collocation points inside each element resulting in a quadrilateral grid with the following properties

$$\begin{aligned} N_p &= 6(N_p^T - 2)N^2 + 2, \\ N_e &= 6(N_p^T - 2), \\ N_s &= 12(N_p^T - 2), \end{aligned} \quad (15)$$

where N_p, N_e , and N_s denote the number of points, elements and sides comprising the quadrilateral grid, and N is the polynomial order used in the semi-discrete discontinuous Galerkin scheme discussed in Sec. 3.1.2.

TABLE I
The number of grid points, elements, and sides for the icosahedral
grid as a function of n_I and N .

n_I	N	$n_I \cdot N$	N_p	N_e	N_s
1	4	4	962	60	120
1	6	6	2162	60	120
1	8	8	3842	60	120
1	12	12	8642	60	120
1	16	16	15362	60	120
1	24	24	34562	60	120
1	32	32	61442	60	120
1	64	64	245762	60	120
<hr/>					
4	1	4	962	960	1920
8	1	8	3842	3840	7680
16	1	16	15362	15360	30720
32	1	32	61442	61440	122880
64	1	64	245762	245760	491520
<hr/>					
2	2	4	962	240	480
4	2	8	3842	960	1920
8	2	16	15362	3840	7680
16	2	32	61442	15360	30720
32	2	64	245762	61440	122880
<hr/>					
1	4	4	962	60	120
2	4	8	3842	240	480
4	4	16	15362	960	1920
8	4	32	61442	3840	7680
16	4	64	245762	15360	30720

Substituting the values in Eq.(14) into Eq.(15) yields

$$N_p = 60(n_I)^2 N^2 + 2, \quad (16)$$

$$N_e = 60(n_I)^2, \quad (17)$$

$$N_s = 120(n_I)^2. \quad (18)$$

Table I provides examples of grids for various values of n_I and N . Examples of corresponding grids for $n_I = 1$ and $N = 4, 8, 16$, and 32 are illustrated in Fig. 2.

5. RESULTS

In the following we evaluate the performance of the scheme discussed in the previous sections. As a measure of the error we use the normalized L_2 error

$$\|\mathbf{q}_N\|_{L_2} = \sqrt{\frac{\int_{\mathbf{D}} (\mathbf{q}_{\text{exact}} - \mathbf{q}_N)^2 d\mathbf{x}}{\int_{\mathbf{D}} \mathbf{q}_{\text{exact}}^2 d\mathbf{x}}}.$$

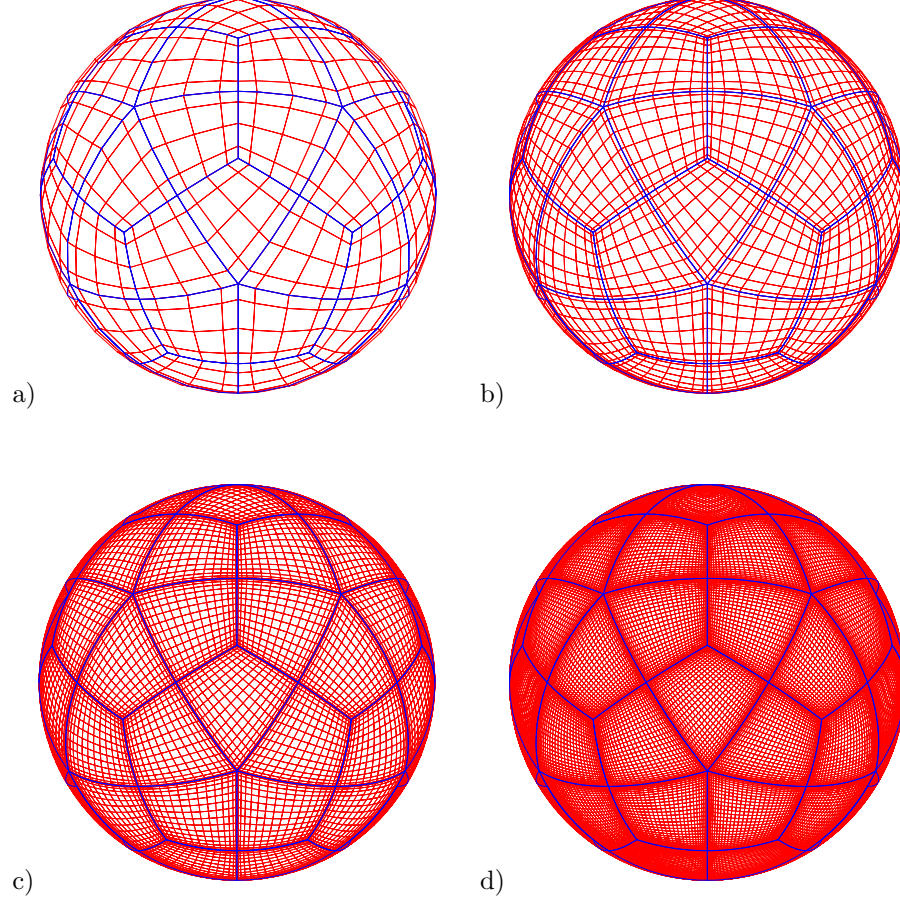


FIG. 2. An icosahedral grid for $n_I = 1$ and a) $N = 4$, b) $N = 8$, c) $N = 16$, and d) $N = 32$.

throughout this section. Here \mathbf{q}_N represents the computed conservation variables and $\mathbf{q}_{\text{exact}}$ the exact when available. The global error is computed as a broken norm using the local quadratures.

Six test cases are used in order to test the algorithms and form a framework for comparison between the two formulations. Cases 1, 2, 3, 5 and 6 correspond to the test cases given in [30]. Case 4 has been used as a test case for the shallow water equations in [8, 9, 20, 21]. Cases 1, 2, and 3 have analytic solutions and are used to evaluate the accuracy of the discontinuous Galerkin method quantitatively. Cases 4, 5, and 6, on the other hand, do not have analytic solutions and are thus used to obtain a qualitative assessment of the accuracy of the scheme.

- *Case 1: Steady-State Advection.* This case concerns the solid body rotation of a cosine wave. It only tests the mass equation as the velocity field is assumed to remain unchanged throughout the computation. The cosine wave completes one full revolution after 12 days of integration.

- *Case 2: Global Steady-State Nonlinear Zonal Geostrophic Flow.* This case is a steady-state solution to the nonlinear shallow water equations. The equations are geostrophically balanced and remain so for the duration of the integration. The velocity field thus remains constant throughout the computation. The geopotential height φ undergoes a solid body rotation but since the initial height field is given as a constant band, the solution remains the same throughout the time integration. The velocity field is the same as that used in Case 1. Williamson et al. [30] recommend that the error be computed after 5 days of integration.

- *Case 3: Steady-State Nonlinear Zonal Geostrophic Flow with Compact Support.* This case is similar to Case 2 except that the velocity is zero everywhere except in a very small isolated region. This isolated region, or jet, encapsulates the flow and limits the geopotential height field to remain within a very confined circular region. As in Case 2, the errors are computed after 5 days.

- *Case 4: Dancing High-Low Waves.* This case comes from [20] and is not an analytic solution to the shallow water equations. The initial geopotential height is comprised of two large waves with the left wave being the low wave and the right wave being the high wave, when viewed from the north pole. The waves rotate clockwise in a swirling dance-like fashion so that after 10 days of integration, the low wave is again on the left and the high wave is on the right.

- *Case 5: Zonal Flow over an Isolated Mountain.* This case is similar to Case 2 except that a mountain has been included on the sphere. This is the only problem in the test cases studied here which includes topography. The mountain is conical in shape and forces the zonal flow to deflect off the mountain. Due to the zonal flow impinging on the mountain, wave structures form and propagate around the sphere. Results are reported for a 10 day integration period.

- *Case 6: Rossby-Haurwitz Wave.* Although Rossby-Haurwitz waves are not analytic solutions to the shallow water equations, they have become a standard test case. In a non-divergent barotropic model, the initial geopotential height field undergoes a solid body rotation in a counterclockwise direction (when viewed from the north pole). Results are reported for a 14 day integration.

In the following we shall use these 6 benchmarks as the stick against which to measure and compare the schemes and their numerical properties such as robustness and accuracy. For the former we shall discuss the impact of various simplifications and approximations introduced into the two schemes, Eqs.(8)-(9), while the latter is evaluated by comparison with exact solutions as well as studies of a more qualitative nature.

5.1. Basic Convergence Tests

Prior to that, however, it seems only natural to discuss and illustrate the advantages of using a high-order scheme for solving the shallow water equations. For this purpose we shall consider the solution of Cases 1, 2, and 3 using the divergence form of the scheme, Eq.(8), only.

Figure 3 shows the computed mass error for the 3 cases using the following orders of accuracy: $N = 1$ (dashed), $N = 2$ (dotted), $N = 4$ (dashed-dotted), and $n_I = 1$ (solid). We plot the mass error norm as a function of the product $n_I N$. The $N = 1$ results are obtained by using linear elements but increasing n_I for increasing

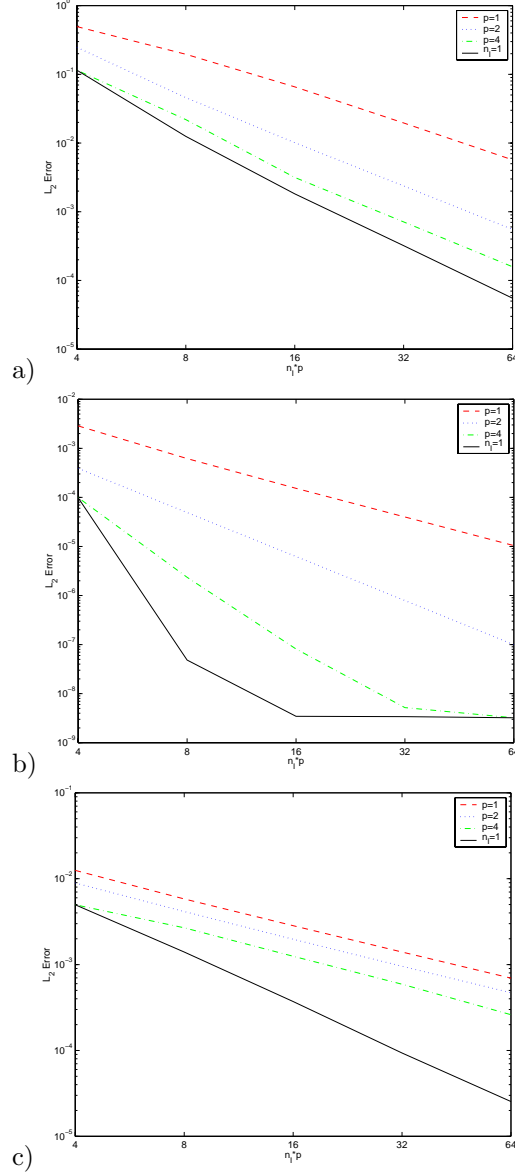


FIG. 3. The mass error norm for the divergence form of the DGM comparing low order schemes ($N \leq 4$) with the N th order scheme ($n_I = 1$) for a) Case 1, b) Case 2, and c) Case 3 for a one day integration.

$n_I N$, i.e., it corresponds to a classic element refinement known as h -refinement. In contrast, the $n_I = 1$ results shown in the plots represent our N th order scheme where we keep the number of elements constant (given by $n_I = 1$) and increase N as is done in classic high-order/spectral convergence.

The results in Fig. 3 confirm the spectral accuracy of the scheme for all three test cases. These results also illustrate well the advantages offered by high-order schemes over low-order schemes in terms of accuracy.

However, it is crucial to understand the cost incurred by this additional accuracy, e.g., if the high-order scheme is prohibitively expensive for levels of accuracy of relevance then the scheme loses much of its appeal.

In order to measure cost versus accuracy, we shall consider the number of operations associated with the different schemes. The simplest reasonable operation count is $\mathcal{O}(N^5 N_e^{3/2})$, where N is the local approximation order on the N_e elements. This estimate is obtained by including the N_e evaluations of the derivatives, being $\mathcal{O}(N^3 N_e)$, and including an additional $\mathcal{O}(N^2 \sqrt{N_e})$ work to account for the number of time-steps required to advance the high-order method. Taking the expression for N_e from Eq.(18), this yields an estimate of the work as $\mathcal{O}(N^5 n_I^3)$.

The main interest is naturally to limit the number of operations needed to achieve a result with a given accuracy, which, on the other hand is a problem dependent entity. Let us first consider the results of Case 1, illustrated in Fig. 3a. Taking an accuracy of 10^{-3} as the goal, it is easily found from Fig. 3a that the 4th order scheme is the one with the least operations, about half that of the 2nd order scheme and almost 5 times less than the first order scheme. In a similar fashion one finds for Case 2 and an accuracy goal of 10^{-6} that the N th order scheme seems most efficient while the 1st and 2nd order methods are prohibitively expensive. For Case 3 and an accuracy goal of 10^{-3} we again find that the N th order scheme appears to be most efficient.

These results provide only guidelines but they do confirm the advantages in using a high-order scheme over lower accuracy methods. Whether one should use the highest order approximation possible or rather limit the order and refine the element size may well be problem dependent. However, as has also been found in other similar studies [9, 12, 13, 15, 26] it is generally advantageous to use a moderate order of approximation, $N = 8 - 16$, and refine the element size accordingly to achieve a practical level of accuracy. Only for problems requiring very high accuracy or long time integration can one benefit from using a very high order scheme, i.e., $N > 16$. The results obtained here support the validity of these guidelines.

5.2. The Divergence Form versus the Green's Form

As a second test we shall evaluate the differences between the divergence form, Eq.(8), and the Green's formulation, Eq.(9), subject to various approximations and simplifications. As a basis for this comparison we shall again use Cases 1, 2, and 3, with the comparisons including the impact of using full or lumped diagonal mass matrices, and the use of exact or inexact integration to compute the discrete operators. Although these differences appear as being small we shall see that the performance of the divergence and Green's formulations can be quite different as a consequence of these differences.

5.2.1. Full versus Diagonal Mass Matrix

One of the most immediate ways of improving the efficiency of the discontinuous Galerkin method is to approximate the mass matrix, M , Eq.(7), by a diagonal (or lumped) form. We form the diagonal approximation of the mass matrix by simply summing all of the entries of each row and storing the sum in the main diagonal.

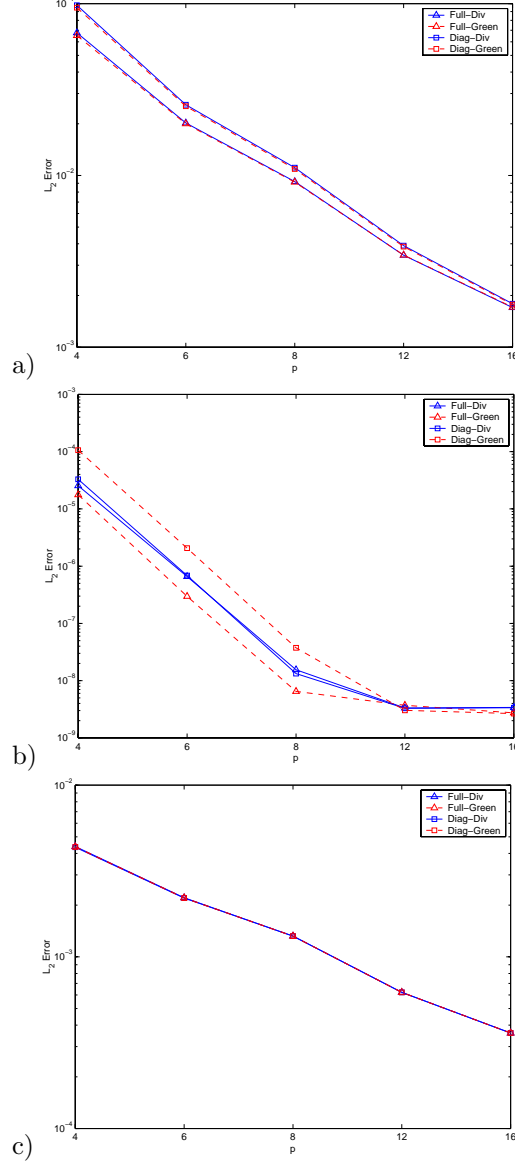


FIG. 4. Evaluation of the φ error induced by using diagonal (square) and full (triangle) mass matrices, M , in the DGM formulations. The error norms are illustrated for the divergence form (solid line) and the Green's form (dashed line) for a) Case 1, b) Case 2, and c) Case 3. All results correspond to one day integrations.

Figure 4 shows the errors obtained using the full and diagonal mass matrices for the divergence and Green's forms, Eqs.(8)-(9), on the $n_I = 1$ grid for Cases 1, 2, and 3.

The results illustrate that the divergence form is generally more robust towards the approximation induced by the diagonal mass matrix, exemplified most clearly by the solution of Case 2. Note, however, that the disparity in accuracy between the full and diagonal forms decreases for all three cases as the order of the basis

functions is increased. The level off of the error decay in Case 2 we attribute to finite precision effects in combination with doing the computations in dimensional variables. This effect, however, does not impact the conclusions.

5.2.2. *Exact versus Inexact Integration*

The evaluation of the discrete operators, e.g., Eq.(7), requires the computations of integrals. Despite the fact that we have the solution defined on Legendre-Gauss-Lobatto quadrature points, the curvilinear geometry, reflected by the transformation Jacobian, and the terms associated with the Coriolis force will create polynomials of higher order and over-integration would be needed to integrate these terms exactly. Indeed, to integrate all of the matrices exactly requires $Q = (cN + 1)/2$ quadrature points, where c is an integer constant denoting the factor of the maximum order matrix. For the spherical shallow water equations $c = 4$, coming from the Coriolis term. For highly skewed elements, however, this factor increases to 6 because of the impact of the transformation Jacobians.

The question to address here is what is the effect of employing inexact integration only, as is done traditionally in continuous spectral element schemes [7, 15, 19, 26]. Here we shall simply use the straightforward quadrature associated with the Legendre-Gauss-Lobatto nodes, to evaluate the inner products and, thus, the discrete operators.

Figure 5 shows the mass error obtained using exact and inexact integration for the matrices of the divergence and the Green's forms on the $n_I = 1$ grid for Cases 1, 2, and 3. Both the divergence and the Green's forms clearly lose accuracy when using inexact integration. Similar to the discussion for the lumped mass matrix, however, we observe that the divergence form appears to be more robust towards such approximations, i.e., the results obtained using the divergence form is always less affected by the approximations than the Green's form. Furthermore, we observe that this increased error level for the Green's form seems to persist for large orders of approximation in Case 2. In other words, the accuracy disparity between the exact and inexact integration of the Green's form appears to not decrease for increased basis function order as it does for the divergence form.

5.2.3. *Divergence versus Green's Form*

The results in Figs. 4 and 5 indicate that the Green's form, Eq.(9), is superior in accuracy to the divergence form, Eq.(8), of the discontinuous Galerkin formulation only if everything is done exactly, i.e., full mass matrices and over-integration to evaluate the discrete operators exactly. However, for all cases, the divergence form performs almost as well even when doing all operations exactly and it was found to be more robust to performance enhancing approximations such as diagonal mass matrices and inexact integration.

Based on these results we shall use the divergence form with inexact integration and diagonal mass matrices for the remainder of the paper as these approximations have a negligible impact on the accuracy. It should be noted, however, that the problems we have considered and on which we have based this choice are limited and it is not clear which formulation to choose for problems of a more general nature, e.g., problems with discontinuous solutions. We hope to address this in future work.

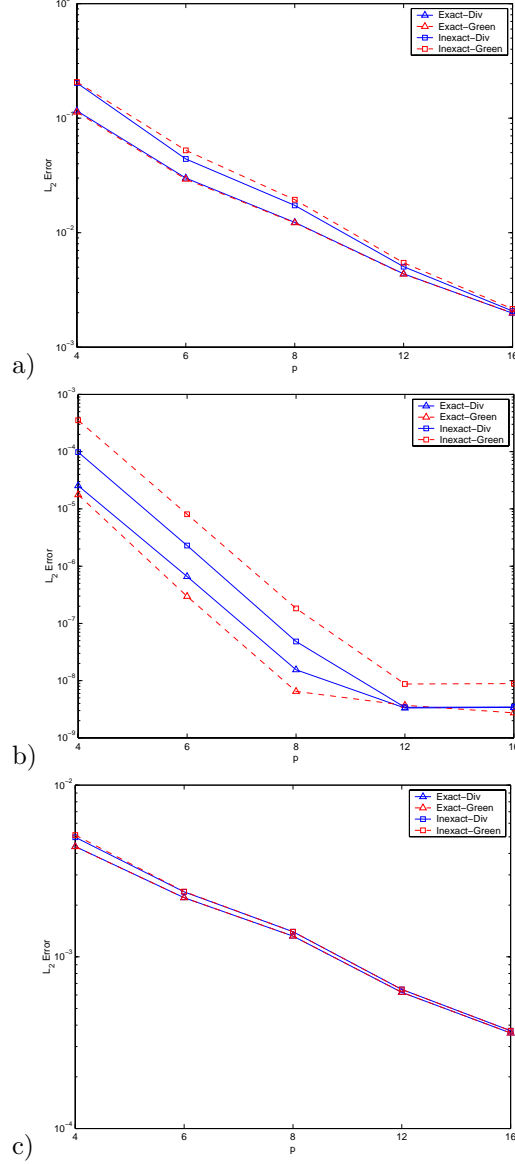


FIG. 5. Evaluation of the φ error induced by using exact (triangle) and inexact (square) integration for the computation of the operators in the DGM formulations. The error norms are illustrated for the divergence form (solid line) and the Green's form (dashed line) for a) Case 1, b) Case 2, and c) Case 3. All results correspond to one day integrations.

5.3. Convergence and Stability Study

In this section we show convergence results for all six cases. Cases 1, 2, and 3 have analytic solutions and so we use these cases to judge the accuracy of our results quantitatively. Cases 4, 5, and 6, on the other hand, are only used to judge the convergence of the scheme qualitatively, as we do not have analytic solutions to these cases. All six test cases are integrated for long periods of time in order to

confirm the stability of the scheme. To ensure stability we apply the Boyd-Vandeven filter after every 10 time steps.

5.3.1. Quantitative Study

Figure 6 shows the mass error norm as a function of the approximation order, N , for Cases 1, 2, and 3. The results for Case 1 are for a 12 day integration which corresponds to a complete revolution of the cosine wave around the sphere. For Cases 2 and 3, the results are for 5 day integrations which is the time frame recommended in [30].

For all cases we observe exponential convergence rates until the effect of the finite precision impacts the solution accuracy. To confirm that the leveling off is due to finite precision effects we have performed studies at a decreased time-step, confirming that the dominating error source is spatial and not temporal.

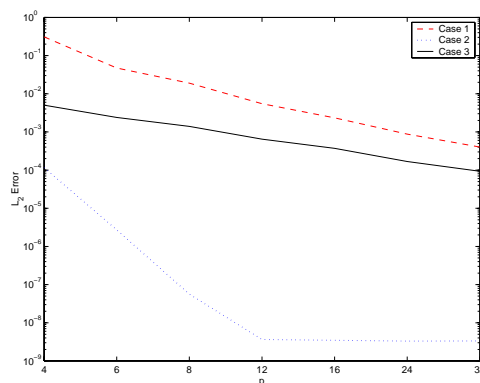


FIG. 6. The φ error as a function of the spatial approximation order, N , for Case 1 (dashed), Case 2 (dotted), and Case 3 (solid) after 12, 5, and 5 days of integrations, respectively. The $n_I = 1$ grid is used.

5.3.2. Qualitative Study

In the previous section we tested cases with analytic solutions against which to compare and judge the accuracy of the schemes. However, the more relevant Cases 4, 5, and 6, do not allow such simple analytic solutions. Instead we shall evaluate the convergence characteristics of the scheme qualitatively by running the cases using different resolutions.

In Figs. 7, 8, and 9 the left panels show the contours of the mass, the middle panels show the zonal velocity component, and the right panels show the meridional velocity component. The zonal velocity component is the u component in spherical coordinates which is associated with the longitude λ and is positive when traveling west to east in a direction parallel to the Equator. The meridional velocity component is the v component in spherical coordinates which is associated with the latitude θ and is positive when traveling from the South Pole to the North Pole.

Figure 7 shows the results for Case 4 using the $n_I = 1$ grid with various orders of approximation, N , for a 10 day integration and confirm that the wave structures remain the same for all three values of N . However the wave pattern clearly becomes better resolved when increasing N . This is most obvious near the North Pole (center

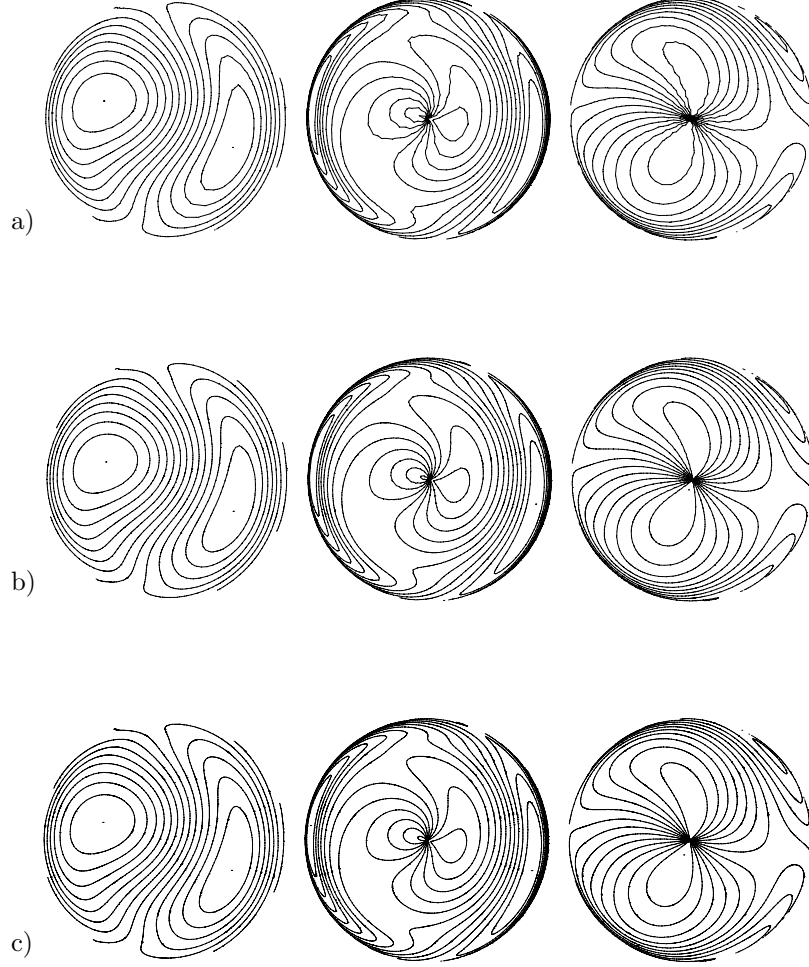


FIG. 7. Case 4. Contours of the mass (left), u-velocity (middle), and v-velocity (right) on grid $n_I = 1$ and a) $N = 8$, b) $N = 16$, and c) $N = 32$ after a 10 day integration viewed from $(\lambda, \theta) = (0, 90)$.

of the plots) for the velocity components. The contours are a bit jagged for $N = 8$ but become smoother for $N = 16$. Finally, for $N = 32$ we see that the same patterns exist as in the $N = 8$ and $N = 16$ contours but the curves are much smoother throughout, indicating a converged result.

Figure 8 shows the results of Case 5 for a 10 day integration using $N = 8, 16$, and 32 , respectively. The contours are shown from the viewpoint $(\lambda, \theta) = (180, 0)$, where the peak of the mountain resides at $(\lambda, \theta) = (180, 30)$. The flow impinging on the mountain causes the resulting wave structures which we see in the figure around the mid-latitudes ($\theta = \pm 45$). The contours for $N = 8$ are again a little jagged - not just for the mass contours but for the velocity components as well. Increasing

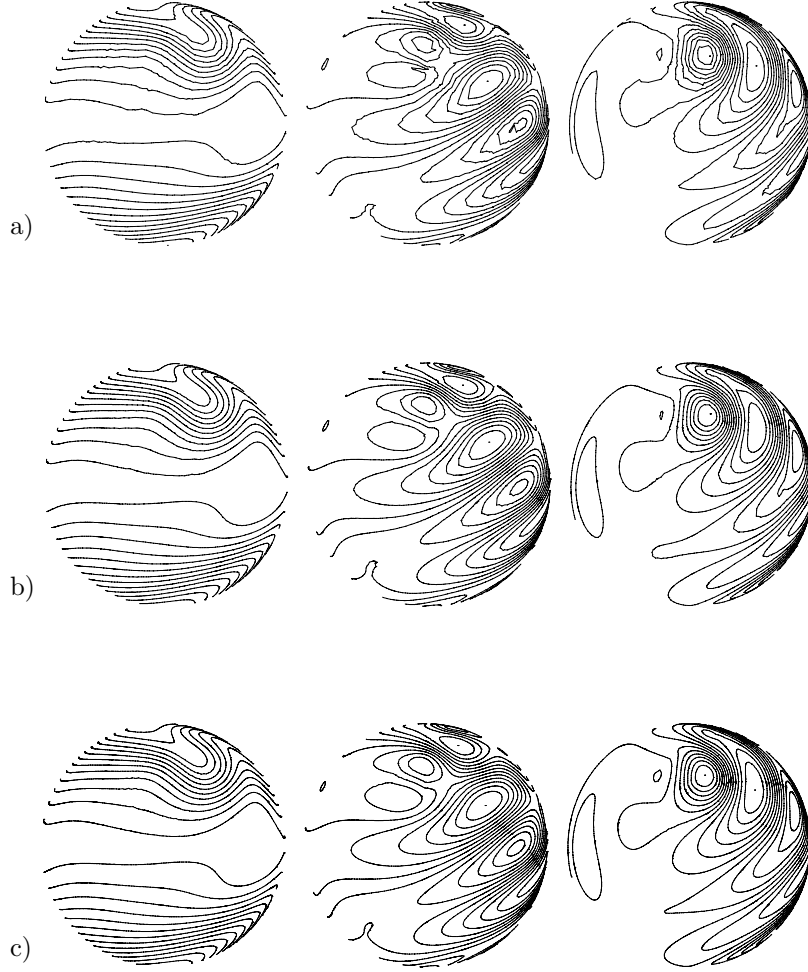


FIG. 8. Case 5. Contours of the mass (left), u-velocity (middle), and v-velocity (right) on grid $n_I = 1$ and a) $N = 8$, b) $N = 16$, and c) $N = 32$ after a 10 day integration viewed from $(\lambda, \theta) = (180, 0)$.

N to 16 removes much of the jaggedness visible in the contours and increasing N further to 32 smoothen the contours completely resulting in clearly visible cohesive wave structures.

Figure 9 shows the results of Case 6 after a 14 day integration at different resolutions with the contours being shown from a viewpoint corresponding to the North Pole $(\lambda, \theta) = (0, 90)$. In contrast to the previous two cases, the results for $N = 8$ show that the wave structures are beginning to break down at this resolution which is insufficient to support the dynamics of the system. This breakdown of the wave structures is most obvious by looking at the mass and velocity field. Increasing N to 16 results in a dramatic improvement with the wave structures becoming more

cohesive. This is particularly noticeable in the mass contours where we see that the rotated Greek cross pattern remains intact instead of breaking off into distinct blobs as in Fig. 9a. Increasing N further to 32 significantly improves the wave patterns. The mass contours for the $N = 16$ scheme are beginning to reveal a semblance of break-off of the wave pattern. This can be seen by looking at the bottom left tip of the cross. For $N = 32$ the wave pattern remains completely intact without any indication of break-off.

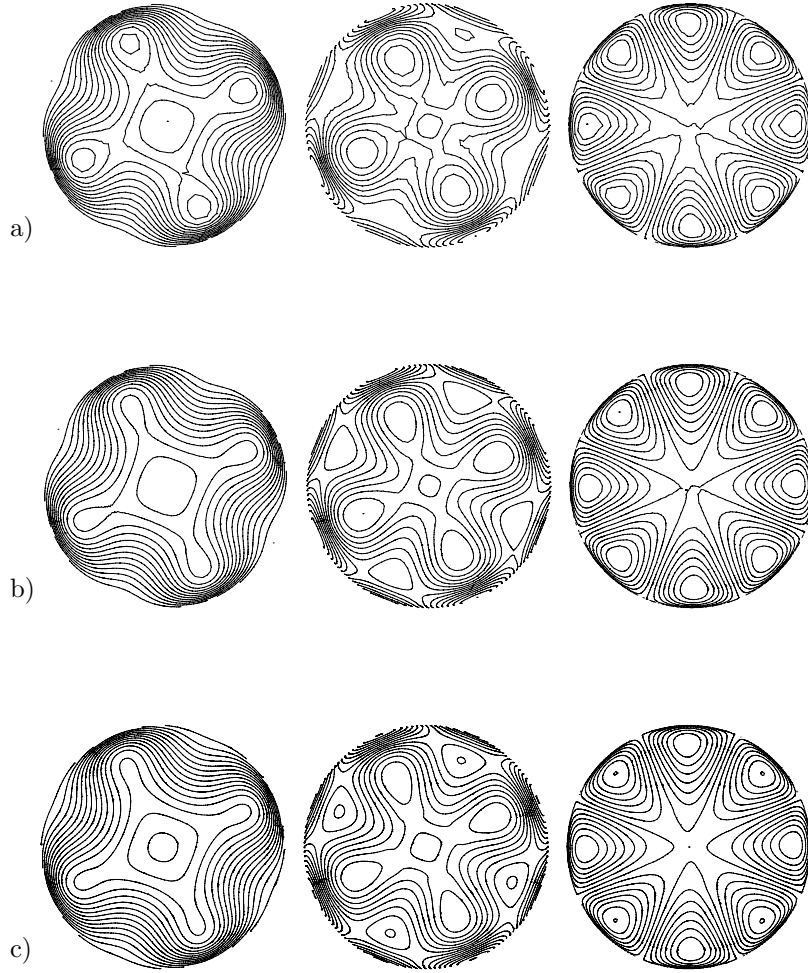


FIG. 9. Case 6. Contours of the mass (left), u-velocity (middle), and v-velocity (right) on grid $n_I = 1$ and a) $N = 8$, b) $N = 16$, and c) $N = 32$ after a 14 day integration viewed from $(\lambda, \theta) = (0, 90)$.

The results for these three cases show that increasing the order of the approximation, N , either improves the smoothness of the contour curves or allows for the resolution of finer scale waves. This is particularly noticeable in Cases 5 and 6. In

Case 5, the velocity components exhibit very localized wave formations that are extremely well resolved by our nodal N th order DGM scheme. Case 6 illustrates the breakdown of the wave structure if insufficient grid resolution is used.

6. CONCLUSIONS

The objective of this paper has been to present the formulation and verification of a high-order accurate nodal discontinuous Galerkin formulation for the solution of the spherical shallow water equations. Curvilinear quadrilateral elements are used to cover the sphere, using an icosahedral grid as the basis for the grid generation, and the equations are solved in Cartesian form to avoid problems with coordinate singularities. On each curvilinear element the solutions are represented by Lagrange polynomials in a purely nodal form, i.e., the solutions are given on quadrature points and operations such as differentiation and integration become matrix-matrix operations. The equations are satisfied in a discontinuous element form with the element continuity being imposed only weakly. This decouples all elements and makes the formulation highly parallel as well as well-suited for adaptive solution techniques as no constraints on element conformity is needed.

The accuracy of the scheme, given in two mathematically equivalent but computationally different forms, has been illustrated by considering the solution of the standard set of benchmarks proposed in [30]. The results confirm the expected high-order/spectral accuracy and illustrate the advantages of using such methods to efficiently solve geophysical flow problems.

To understand, however, whether the approach proposed here provides a realistic alternative to existing methods based on spherical harmonics or continuous spectral element methods requires extensive further validation. The inherent properties of the proposed technique, e.g., high parallel efficiency, high-order accuracy and support for adaptive, non-conforming solution techniques, are sufficient to warrant such exhaustive studies and we hope to report on such results in the near future.

ACKNOWLEDGMENT

The first author (FXG) gratefully acknowledges his sponsor, the Office of Naval Research, which supported this work through program element PE-0602435N. The two last authors acknowledge partial support of AFOSR/DARPA under contract F49620-1-0426. The second author (JSH) also acknowledge support by the Alfred P. Sloan Foundation as a Sloan Research Fellow and, furthermore, wishes to express his gratitude for the hospitality of the Department of Mathematical Modeling at the Technical University of Denmark in August 2001 during which parts of the present work were completed.

REFERENCES

1. F. Bassi and S. Rebay, High-order accurate discontinuous finite element solution of the 2D Euler equations, *Journal of Computational Physics* **138**, 251-285 (1997).
2. K.S. Bey and J.T. Oden, hp-version discontinuous Galerkin methods for hyperbolic conservation laws, *Computer Methods in Applied Mechanics and Engineering* **133**, 259-286 (1996).
3. J. Boyd, The erfc-log filter and the asymptotics of the Euler and Vandeven sequence accelerations, *Houston Journal of Mathematics* (1996).
4. B. Cockburn and C.W. Shu, The Runge-Kutta discontinuous Galerkin method for conservation laws: V. multidimensional systems, *Journal of Computational Physics* **141**, 199-224 (1998).
5. B. Cockburn and C.W. Shu, Runge-Kutta Discontinuous Galerkin Methods for Convection-Dominated Problems, *Journal of Scientific Computing*, 2001 – to appear.

6. B. Engquist and S. Osher, One-sided difference approximations for nonlinear conservation laws, *Mathematics of Computations* **36**, 321-352 (1981).
7. F.X. Giraldo, Lagrange-Galerkin spectral element methods on unstructured quadrilateral grids, *Journal of Computational Physics* **147**, 114-146 (1998).
8. F.X. Giraldo, Lagrange-Galerkin methods on spherical geodesic grids: the shallow water equations, *Journal of Computational Physics* **160**, 336-368 (2000).
9. F.X. Giraldo, A spectral element shallow water model on spherical geodesic grids, *International Journal for Numerical Methods in Fluids* **35**, 869-901 (2001).
10. D. Gottlieb and J. S. Hesthaven, Spectral Methods for Hyperbolic Problems, *Journal of Computational and Applied Mathematics*, **128**, 83-131 (2001).
11. J.J. Hack, B.A. Boville, B.P. Briegleb, J.T. Kiehl, P.J. Rasch, and D.L. Williamson, Description of the NCAR community climate model (CCM2), NCAR Technical Note NCAR/TN-382+STR, National Center for Atmospheric Research, Boulder, CO. (1992).
12. J. S. Hesthaven, A Stable Penalty Method for the Compressible Navier-Stokes Equations. II. One-Dimensional Domain Decomposition Schemes, *SIAM J. Sci. Comp.* **18**, 658-685, 1997.
13. J. S. Hesthaven, A Stable Penalty Method for the Compressible Navier-Stokes Equations. III. Multi Dimensional Domain Decomposition Schemes, *SIAM J. Sci. Comp.* **20**, 62-93, 1999.
14. T.F. Hogan and T.E. Rosmond, The description of the Navy operational global atmospheric prediction systems spectral forecast model, *Monthly Weather Review* **119**, 1786-1815 (1991).
15. M. Iskandarani, D.B. Haidvogel, and J.P. Boyd, Staggered spectral element model with application to the oceanic shallow water equations, *International Journal for Numerical Methods in Fluids* **20**, 393-414 (1995).
16. R. Jakob-Chien, J.J. Hack, and D.L. Williamson, Spectral transform solutions to the shallow water test set, *Journal of Computational Physics* **119**, 164-187 (1995).
17. J. Levin, M. Iskandarani, and D.B. Haidvogel, A nonconforming spectral element ocean model, *International Journal for Numerical Methods in Fluids* **34**, 495-525 (2000).
18. J.G. Liu and C.W. Shu, A high-order discontinuous Galerkin method for 2D incompressible flows, *Journal of Computational Physics* **160**, 577-596 (2000).
19. H. Ma, A spectral element basin model for the shallow water equations, *Journal of Computational Physics* **109**, 133-149 (1993).
20. A. McDonald and J.R. Bates, Semi-Lagrangian integration of a gridpoint shallow water model on the sphere, *Monthly Weather Review* **117**, 130-137 (1989).
21. B. Neta, F.X. Giraldo, and I.M. Navon, Analysis of the Turkel-Zwas scheme for the two-dimensional shallow water equations in spherical coordinates, *Journal of Computational Physics* **133**, 102-112 (1997).
22. J. Pedlosky, *Geophysical Fluid Dynamics*, Springer-Verlag, New York (1987).
23. P.L. Roe, Approximate Riemann solvers, parameter vectors and difference schemes, *Journal of Computational Physics* **43**, 357-372 (1981).
24. J.G. Sela, Spectral modeling at the National Meteorological Center, *Monthly Weather Review* **108**, 1279-1292 (1980).
25. A.J. Simmons, D.M. Burridge, M. Jarraud, C. Girard, and W. Wergen, The ECMWF medium-range prediction models development of the numerical formulations and the impact of increased resolution, *Meteorology and Atmospheric Physics* **40**, 28-60 (1989).
26. M. Taylor, J. Tribbia, and M. Iskandarani, The spectral element method for the shallow water equations on the sphere, *Journal of Computational Physics* **130**, 92-108 (1997).
27. H.M. Tufo and P.F. Fischer, Terascale Spectral Element Algorithms and Implementations, in *Proceedings of the ACM/IEEE SC99 Conference on High Performance Networking and Computing*. IEEE Computer Society, CDROM (1999).
28. B. Van Leer, Towards the ultimate conservative difference scheme. V: A second order sequel to Godunov's method, *Journal of Computational Physics* **32**, 101-136 (1979).
29. H. Vandeven, Family of spectral filters for discontinuous problems, *Journal on Scientific Computing* **6**, 159-192 (1991).
30. D.L. Williamson, J.B. Drake, J.J. Hack, R. Jakob, and P.N. Swarztrauber, A standard test set for numerical approximations to the shallow water equations in spherical geometry, *Journal of Computational Physics* **102**, 211-224 (1992).